Supplementary Material

Biomechanical Consequences of Compromised Elastic Fiber Integrity and Matrix Cross-Linking on Abdominal Aortic Aneurysmal Expansion

D. Weiss[a*], M. Latorre[a*], B.V. Rego[a], C. Cavinato[a], B.J. Tanski[b], A.G. Berman[b],
C.J. Goergen[b], J.D. Humphrey[a,c]

[a]Department of Biomedical Engineering
Yale University, New Haven, CT
[b]Weldon School of Biomedical Engineering
Purdue University, West Lafayette, IN
[c]Vascular Biology and Therapeutics Program
Yale School of Medicine, New Haven, CT

[*]These authors contributed equally

Author for correspondence:

J.D. Humphrey, Ph.D.
Department of Biomedical Engineering
Malone Engineering Center
Yale University, New Haven, CT 06520 USA
jay.humphrey@yale.edu
+1-203-432-6428

Figures and Tables

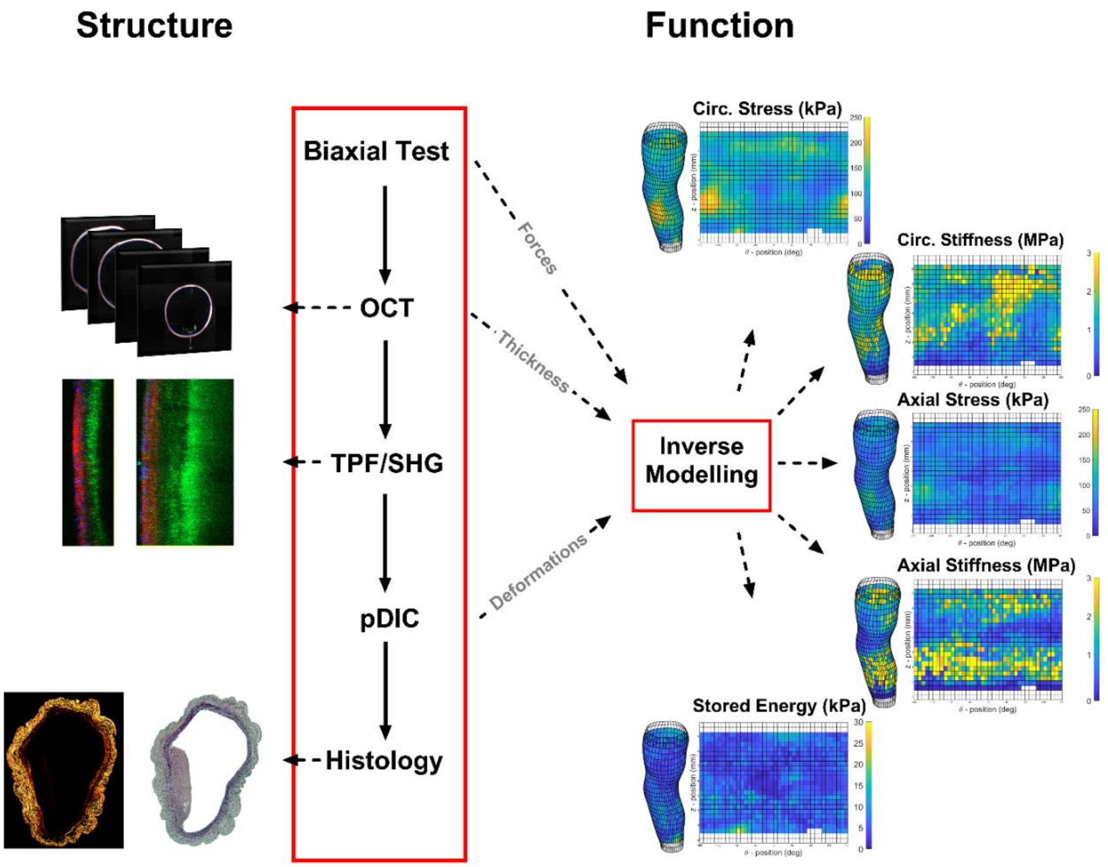

Figure S1. Workflow. Following *in vivo* ultrasound assessments (Figure S2 - top), the infrarenal aortas were excised, cleaned, and mounted within a custom biaxial system to perform cyclic force-length tests at four fixed pressures and cyclic pressure-diameter tests at three sample-specific lengths, *in vivo* and ± 5% that value. The samples were then re-cannulated on a custom triple-needle assembly and scanned using an Optical Coherence Tomography (OCT) system to quantify wall thickness along the entire length. Still mounted on this needle assembly, the samples were then imaged using multi-photon microscopy to generate two-photon fluorescence (TPF) images of elastin (green) and second harmonic generation (SHG) images of collagen (red), with cell nuclei captured as well (blue). Next, a distinct speckle pattern (white dots on a dark background) was formed on the adventitial surface and its reflection on a conical mirror was tracked from eight different views at 42 quasi-static configurations associated with different pressures and axial stretches. Panoramic digital image correlation (pDIC) enabled quantification of the 3D geometry and surface displacement in each state relative to a single reference (80 mmHg, *in vivo* axial stretch). These deformations together with thicknesses from OCT plus pressures and axial forces measured during the standard biaxial testing at particular axial stretches were used in an inverse characterization to determine local biomechanical properties regionally (800-1000 regions, or elements, per sample). Finally, the samples were fixed in formalin and stained for histological examination. The 3D reconstruction of one lesion is shown on the right in the reference configuration, with key biomechanical metrics mapped onto the 3D surface as well as shown in an unwrapped 2D representation.

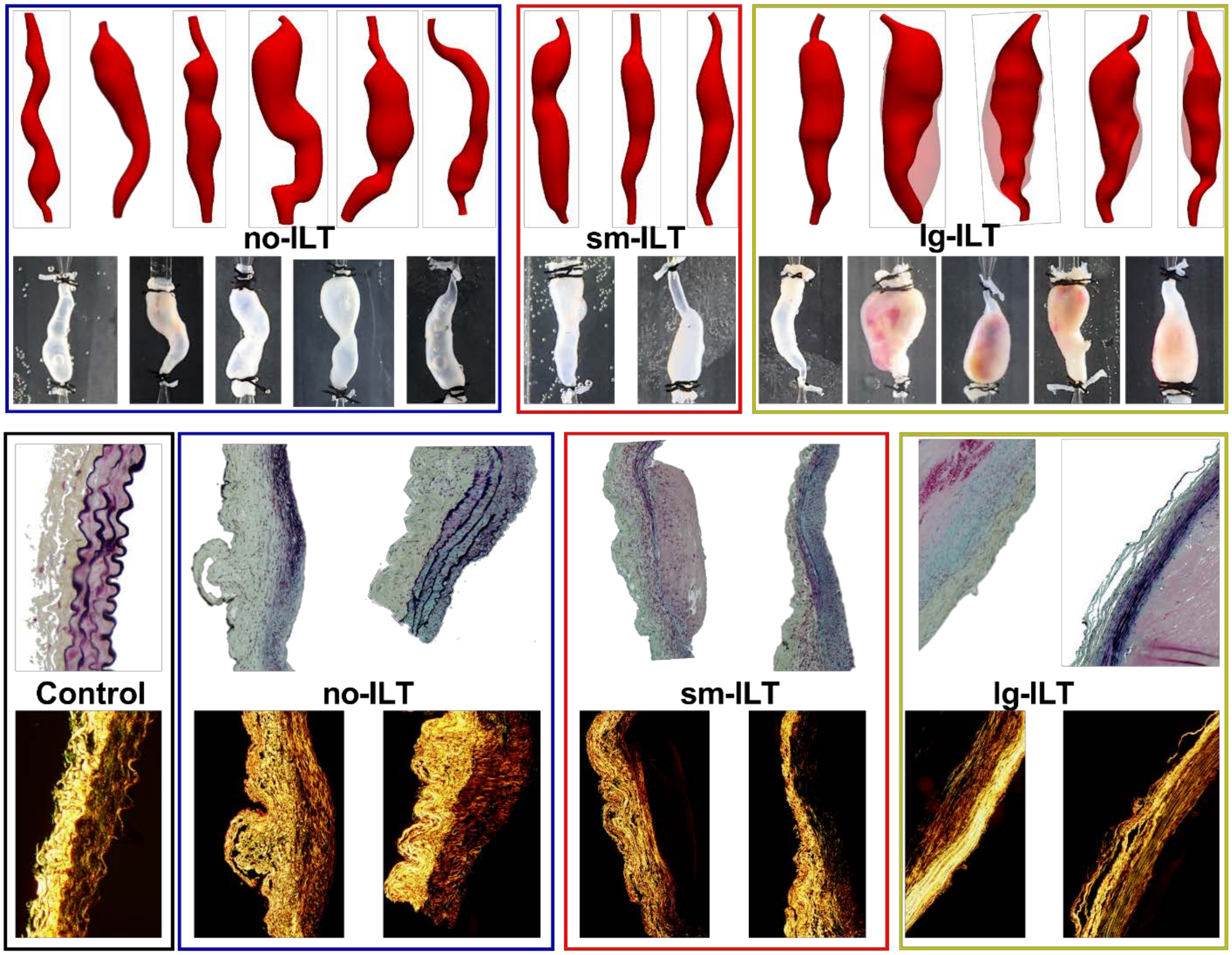

Figure S2. The *in vivo* geometry of all 14 abdominal aortic aneurysms that were tested *in vitro* was segmented manually (luminal and adventitial surfaces) from 3D ultrasound datasets using SimVascular (simvascular.org), as seen in the first row, with intraluminal thrombus (ILT) denoted in pink. Also shown are most of the corresponding excised segments (second row) following cannulation with custom-drawn glass micropipettes, ligation (black 6-0 sutures at the edges of each sample), and placement within the standard biaxial system. Note that one video screen save image is missing from the no-ILT and the sm-ILT groups. Representative Movat-stained sections (third row) revealed damage to the elastin structure (black) in the aneurysms compared with the compact lamellar structure in the control (left) as well as a marked accumulation of glycosaminoglycans (blue) in the aneurysms. Cytoplasm (violet) was abundant in the medial layer of the controls, but scarce in the other groups; significant fibrin (light pink) existed in the sm-ILT and lg-ILT groups. Picro-sirius red stained sections viewed under polarized light (fourth row), for the corresponding Movat sections, showed increased adventitial collagen from control to no-ILT samples, followed by a decrease in the lg-ILT group, for which the collagen also appeared thin and stretched.

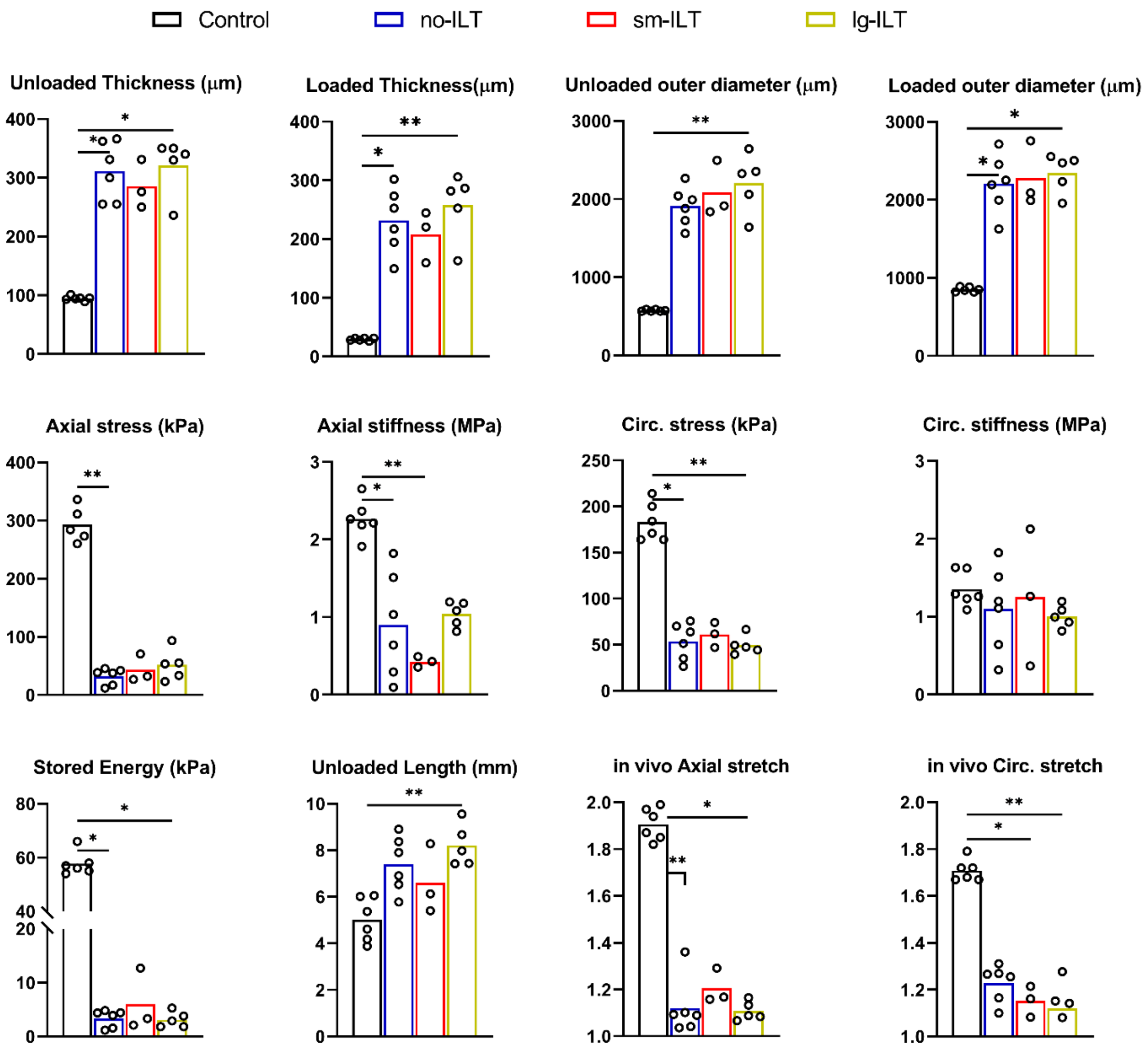

Figure S3. Geometrical and biaxial mechanical metrics for the four primary study groups (see Figure 1 in the main text) determined via standard computer-controlled biaxial mechanical testing. Load-dependent metrics were computed at the sample-specific *in vivo* value of axial stretch and a common distending pressure of 120 mmHg (consistent with tail-cuff measurements of mean systolic pressures). Note that this *in vivo* value of axial stretch is taken as that value at which the transducer-measured axial force does not change appreciably during cyclic pressurization, which appears to be energetically preferred. Importantly, there was a dramatic increase in both mean wall thickness and outer diameter and a dramatic decrease in the *in vivo* axial stretch in all of the elastase+BAPN groups (no-ILT, sm-ILT, lg-ILT), with associated marked reductions in the mean biaxial wall stresses and elastic energy storage compared with the control. **p<0.01, *p<0.05.

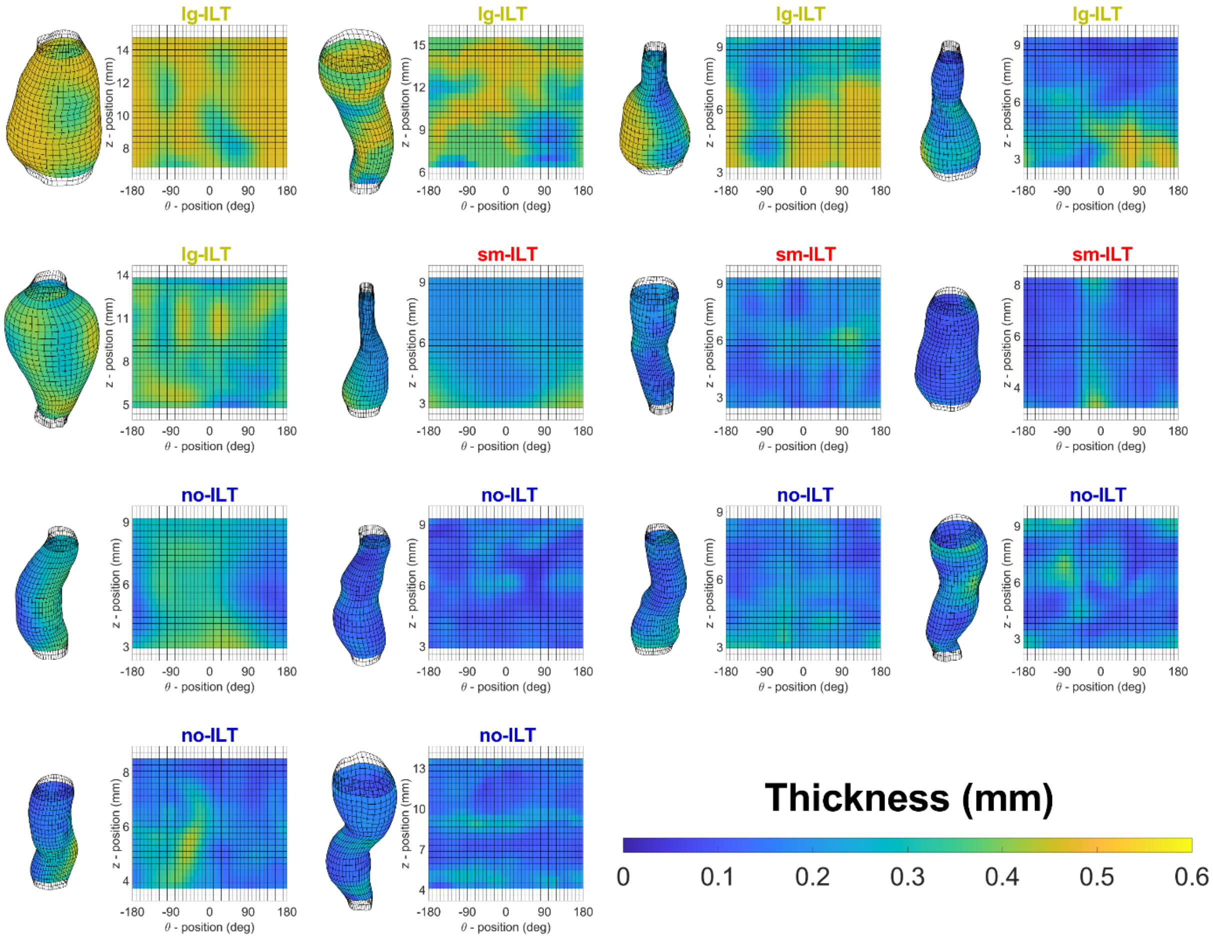

Figure S4. Sample-specific maps of wall thickness determined using Optical Coherence Tomography (OCT), but projected onto 3D surfaces that were generated individually for each of the 14 aneurysmal samples using panoramic Digital Image Correlation (pDIC). These 3D surfaces were also unwrapped to allow projections onto 2D circumferential-axial planes. The values of wall thickness (mm) are shown at a common pressure of 80 mmHg, but at specimen-specific *in vivo* axial stretches. This configuration served as the reference in all pDIC measurements shown below.

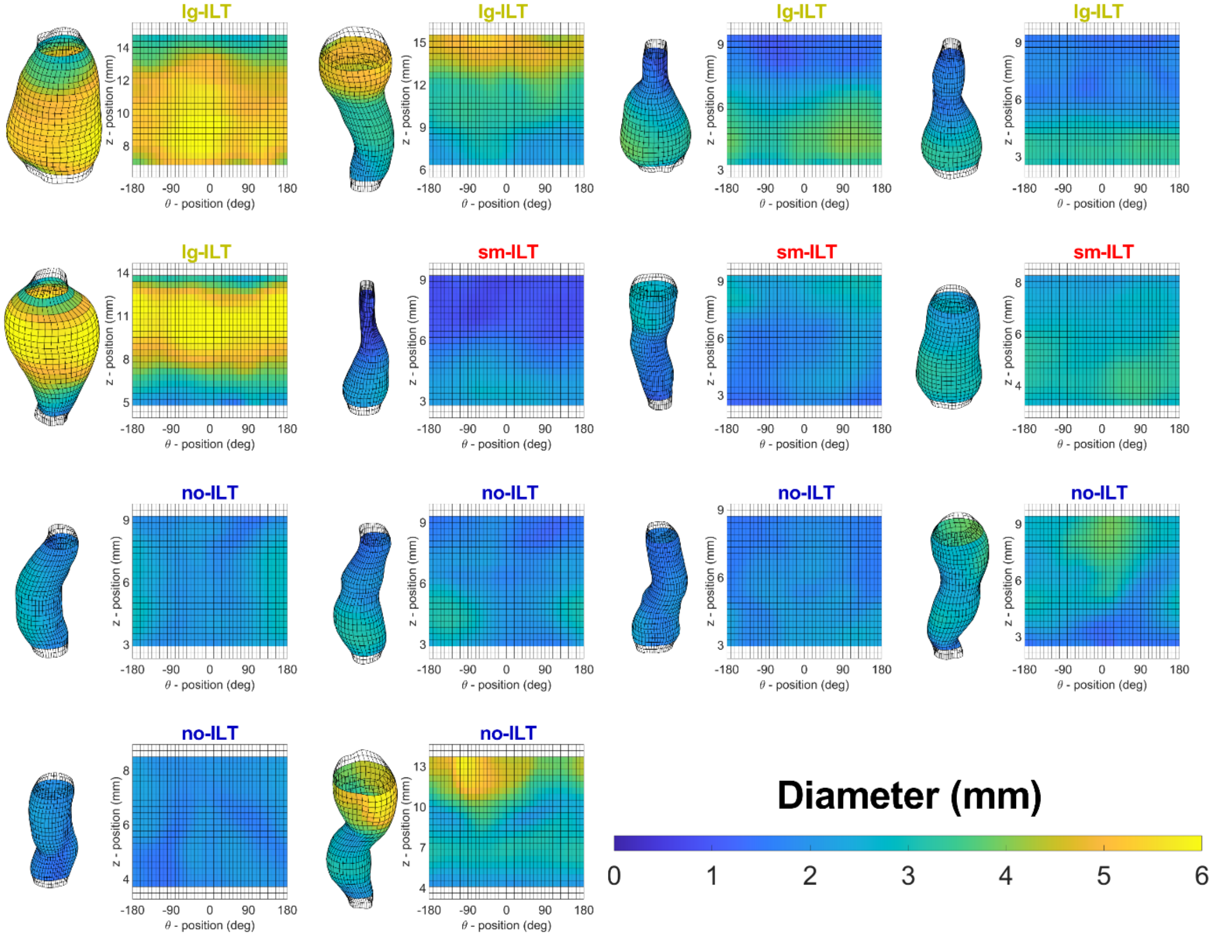

Figure S5. Sample-specific maps of outer diameter obtained via panoramic Digital Image Correlation (pDIC). Diameter (mm) within each quadrilateral computational element was computed at a common distending pressure of 80 mmHg but the specimen-specific *in vivo* axial stretch (reference configuration), then superimposed on the corresponding reconstructed sample geometry (3D maps) or unwrapped and projected onto a θ-Z plane (2D maps) around the vessel circumference (θ ∈ [-180,180] degrees) and along its (Z, distance in mm) axial extent. The ends of the samples were not analyzed to avoid end-effects due to the ligatures/sutures that secured the samples on the needle assembly.

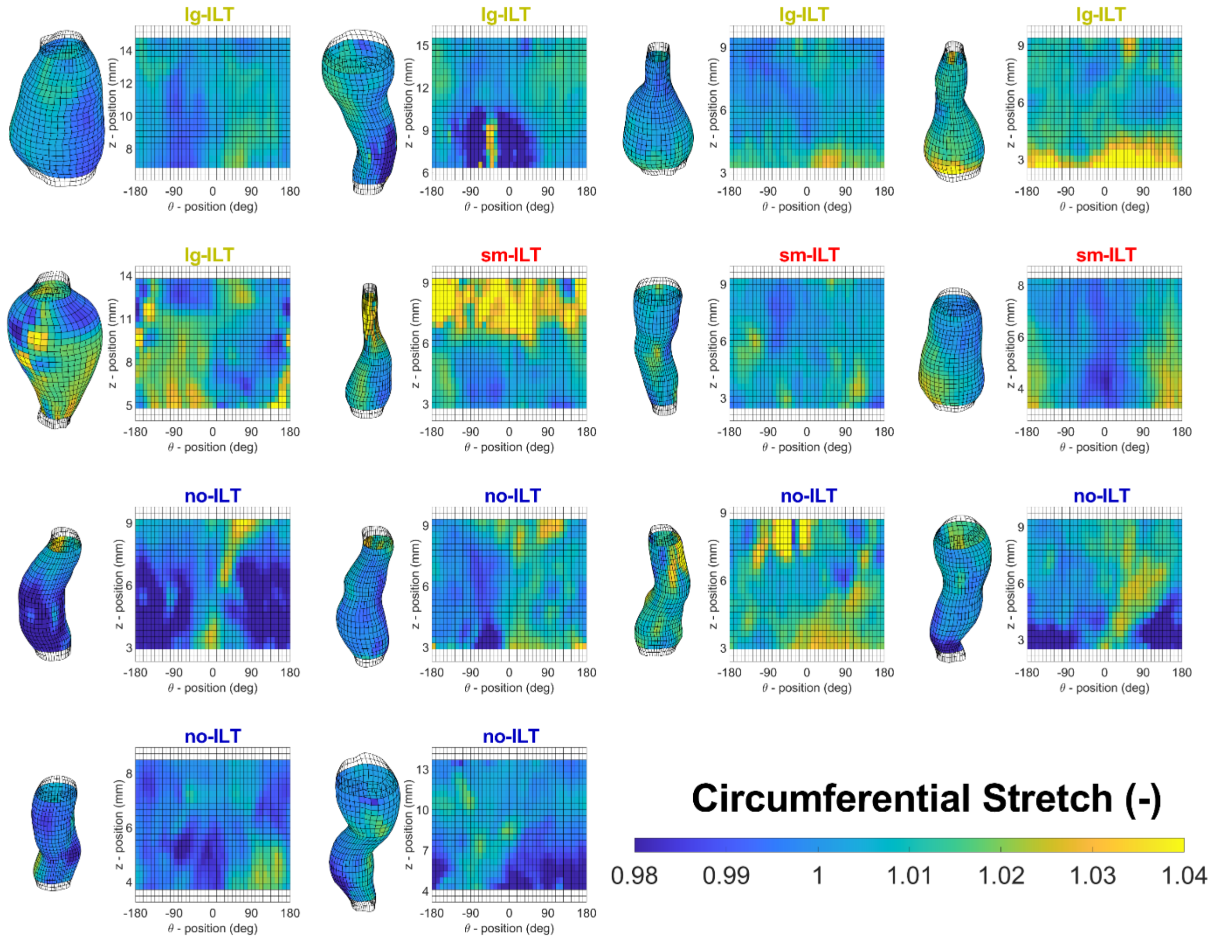

Figure S6. Similar to Figure S5, except for circumferential stretch. Values were computed at 120 mmHg relative to the reference configuration (80 mmHg), both at the specimen-specific axial stretch. Note, for example, the local distribution in the first sm-ILT sample (second row, second column) where the aneurysmal region is barely stretched compared to the more distended (near normal) region, consistent with an increased circumferential stiffness for the aneurysmal wall (see Figure S10).

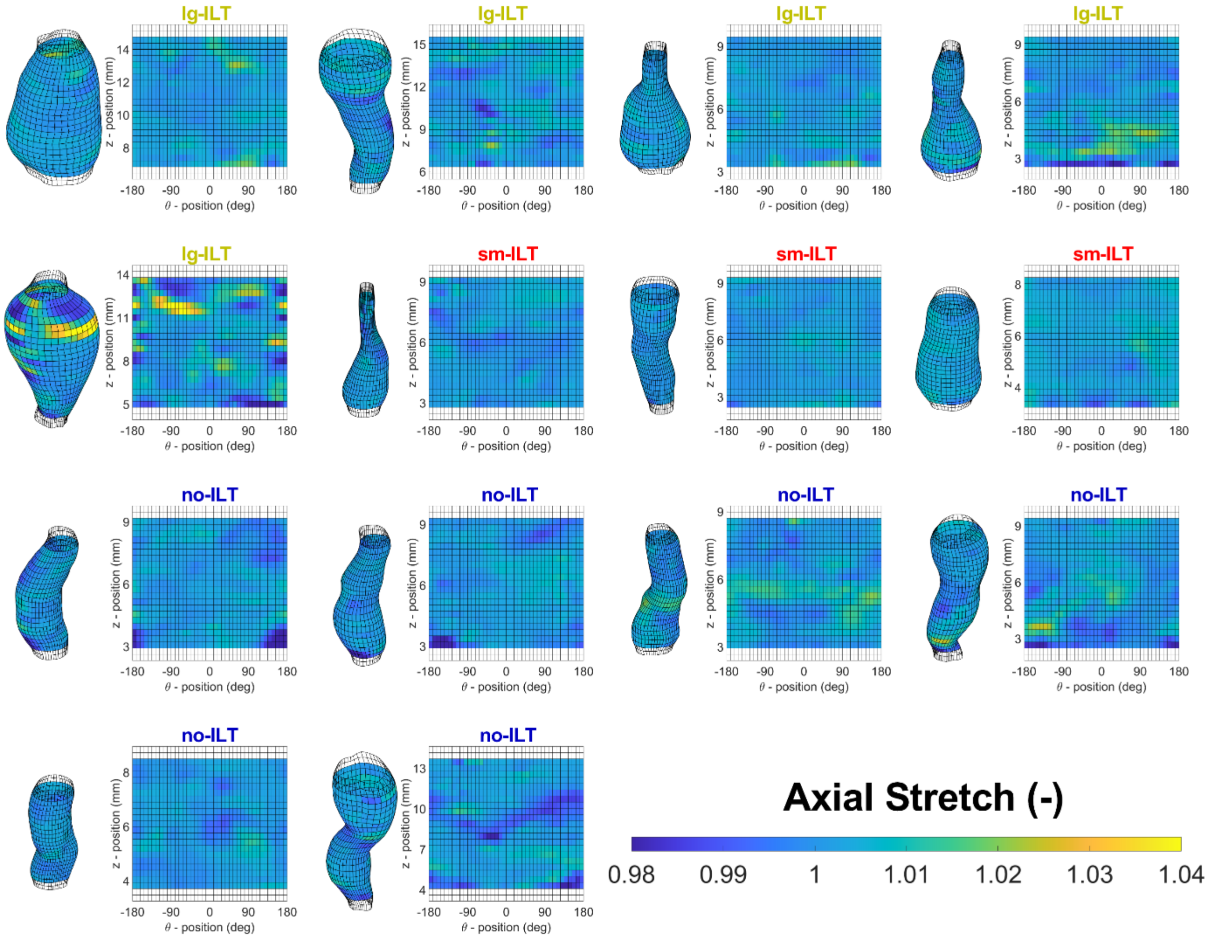

Figure S7. Same as Figure S6, except for (local) axial stretch. Values were computed at 120 mmHg relative to the reference configuration (80 mmHg), both at the specimen-specific (end-to-end) axial stretch. Axial stretches were generally low across all regions of the aneurysms. For comparison, see Figure S3 for control values.

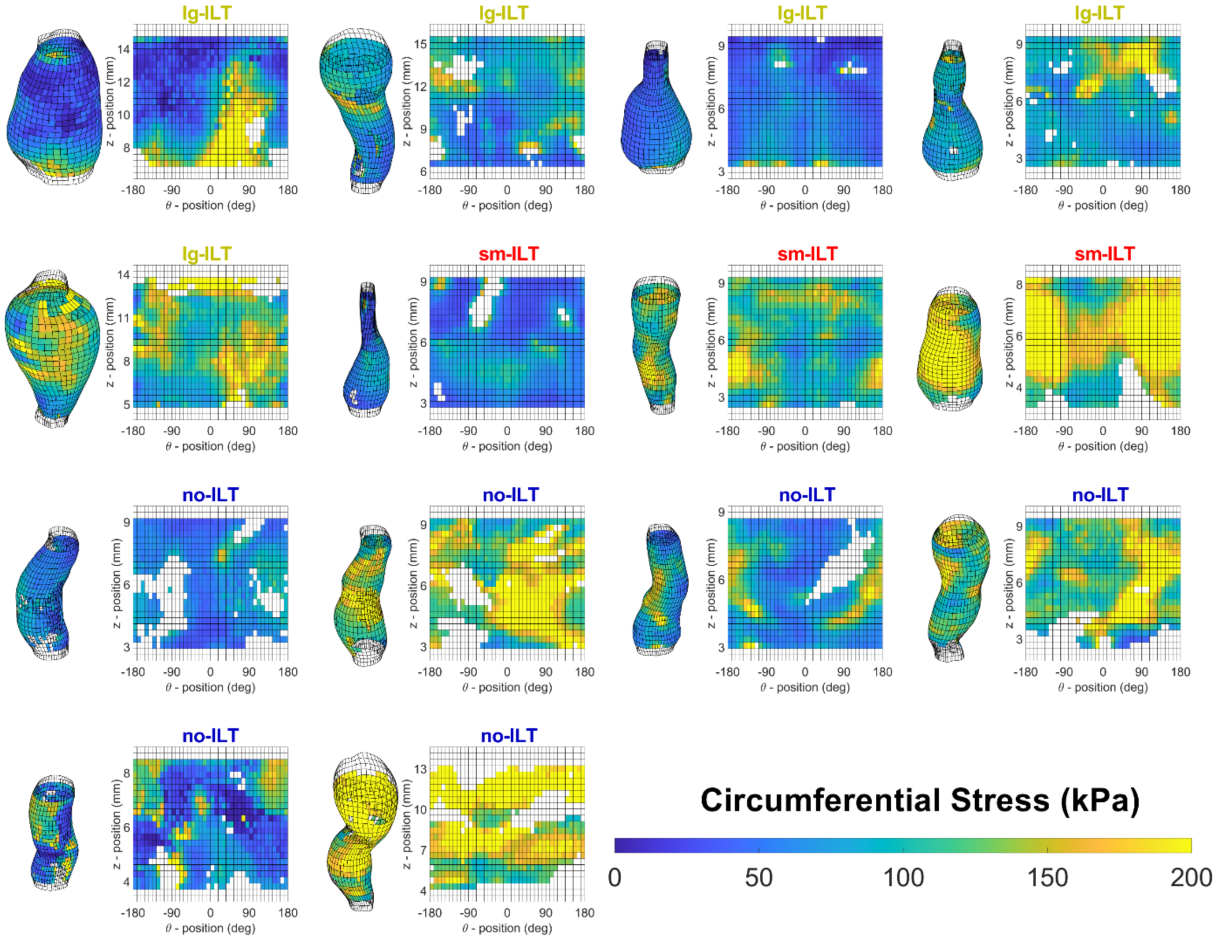

Figure S8. Similar to Figure S5, except for circumferential Cauchy stress (kPa). Virtual field-based inverse characterization allowed these values to be computed at any state, shown here for a common pressure of 120 mmHg but the specimen-specific axial stretch. Note the heterogenous distributions in most of the samples. Elements with a poor coefficient of determination were neglected and left blank.

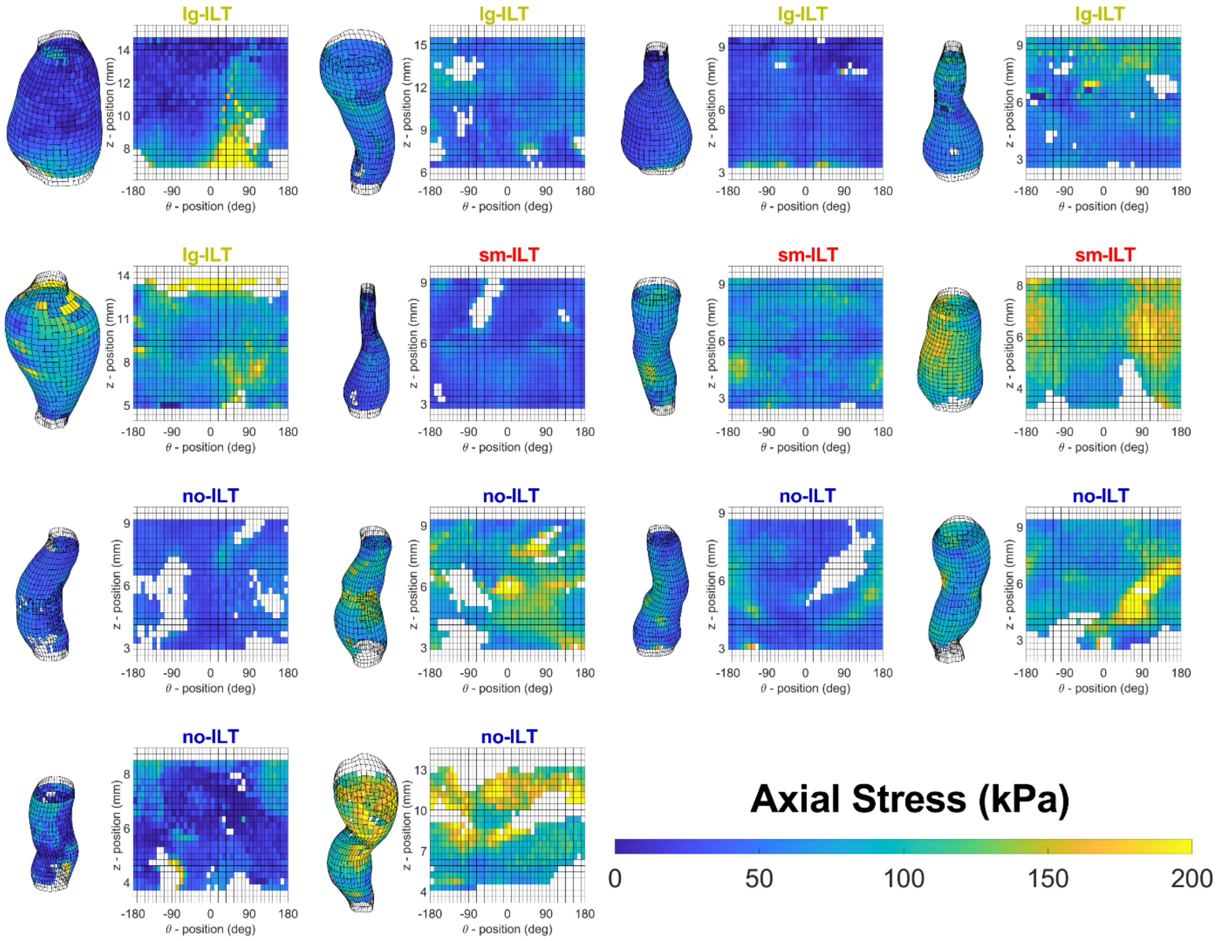

Figure S9. Same as Figure S8, except for axial Cauchy stress (kPa). Virtual field-based inverse characterization allowed these values to be computed at any state, shown here for a common pressure of 120 mmHg but the specimen-specific axial stretch. Elements with a poor coefficient of determination were neglected and left blank.

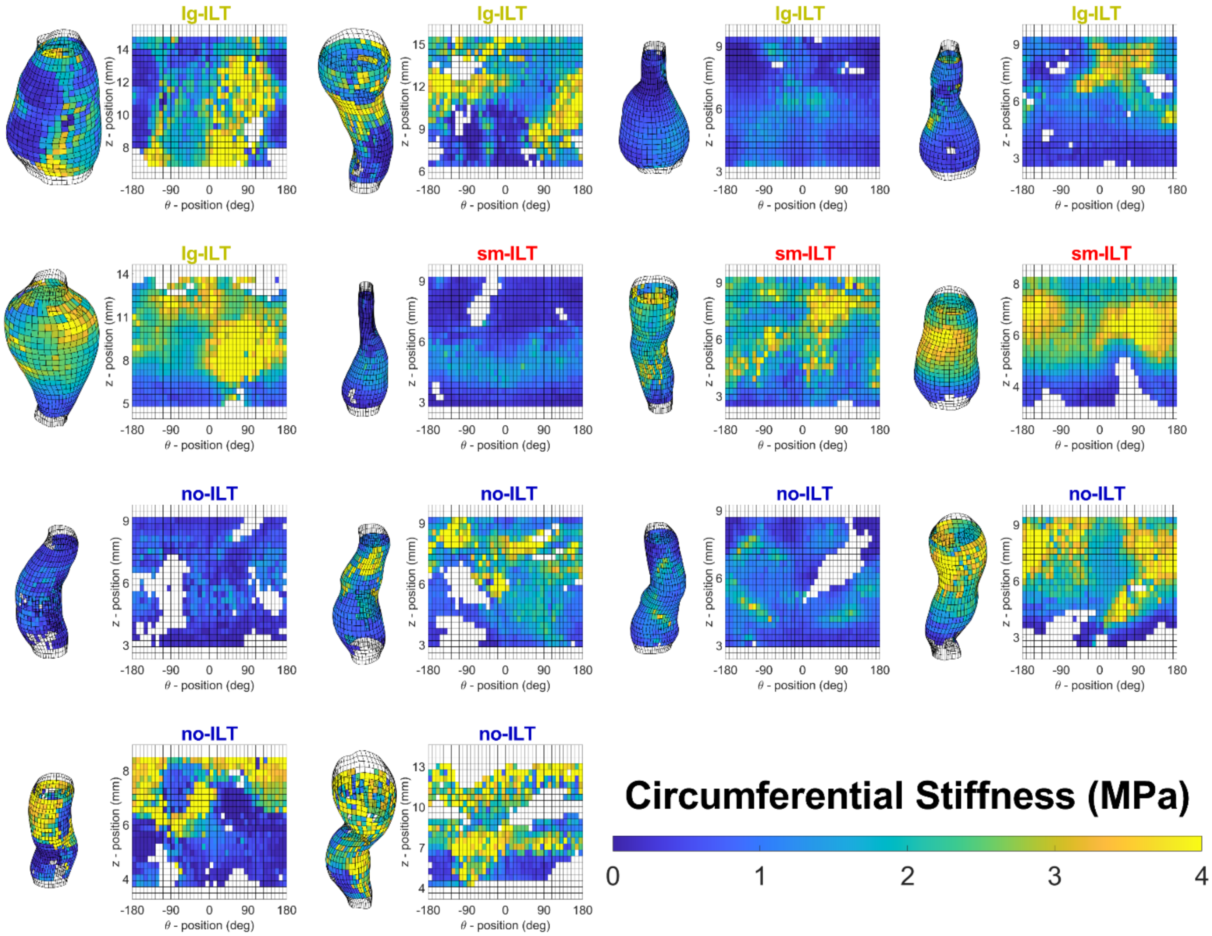

Figure S10. Specimen-specific circumferential material stiffness (MPa) maps. Values were calculated based on local material parameters identified in the inverse characterization, but linearized using the theory of small deformations on large (about at a common pressure of 120 mmHg but specimen-specific axial stretch), which yields values having utility in fluid-solid-interaction simulations, among others.

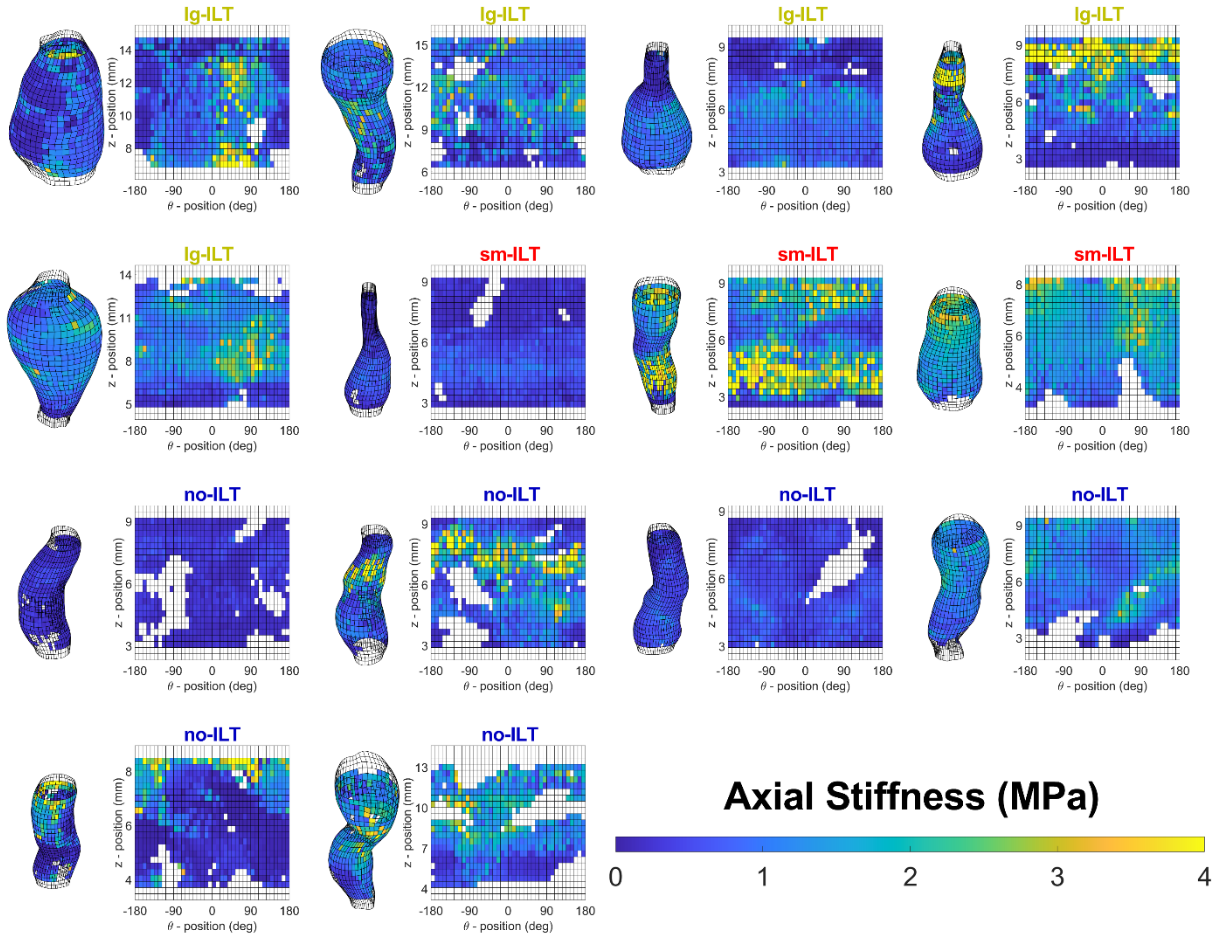

Figure S11. Same as Figure S10, but for axial material stiffness (MPa).

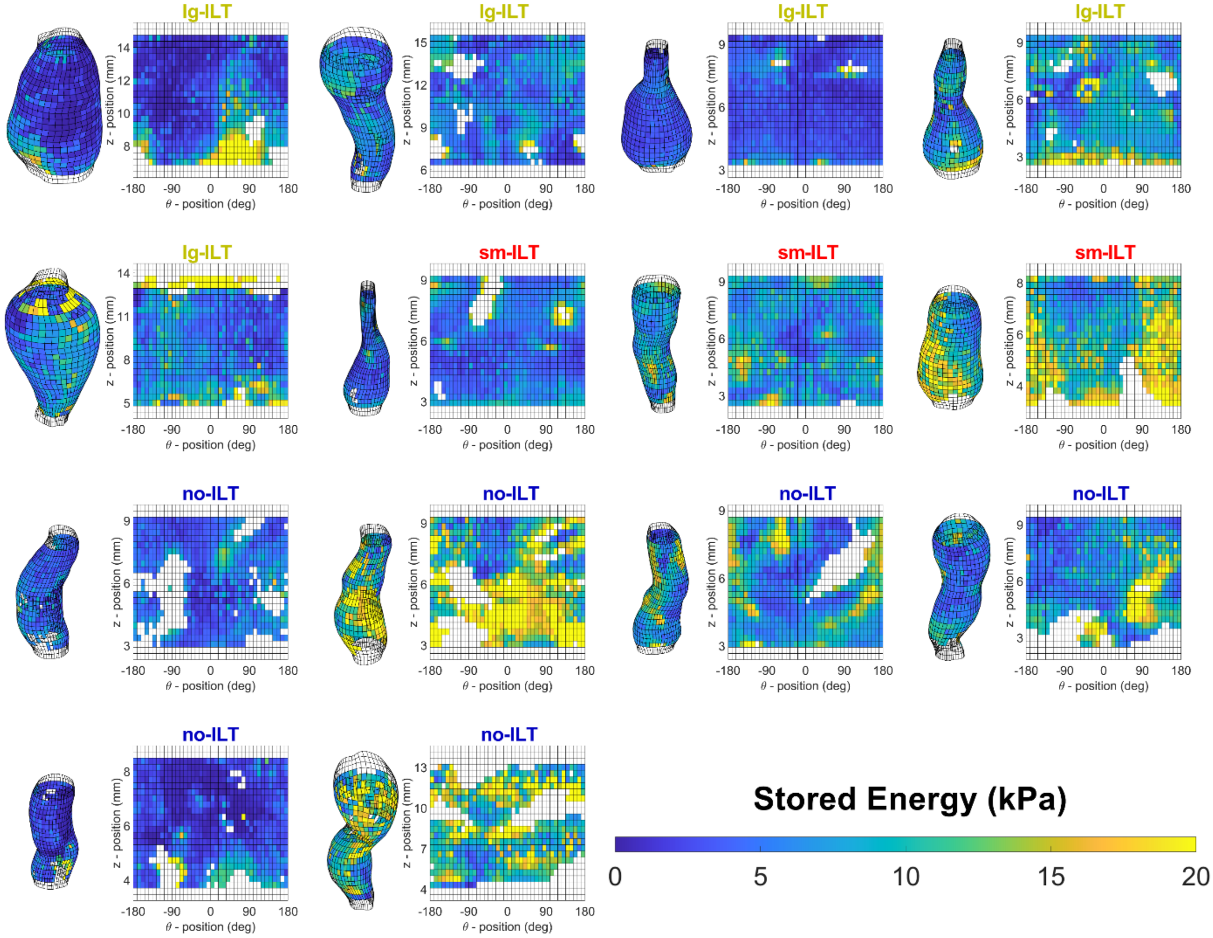

Figure S12. Same as Figures S10-S11, but for elastically stored energy. Note that energy storage is generally a good metric for elastic fiber function and integrity. As evident here, energy storage was very low for all aneurysms (likely due to the elastase exposure and loss of elastic fiber integrity).

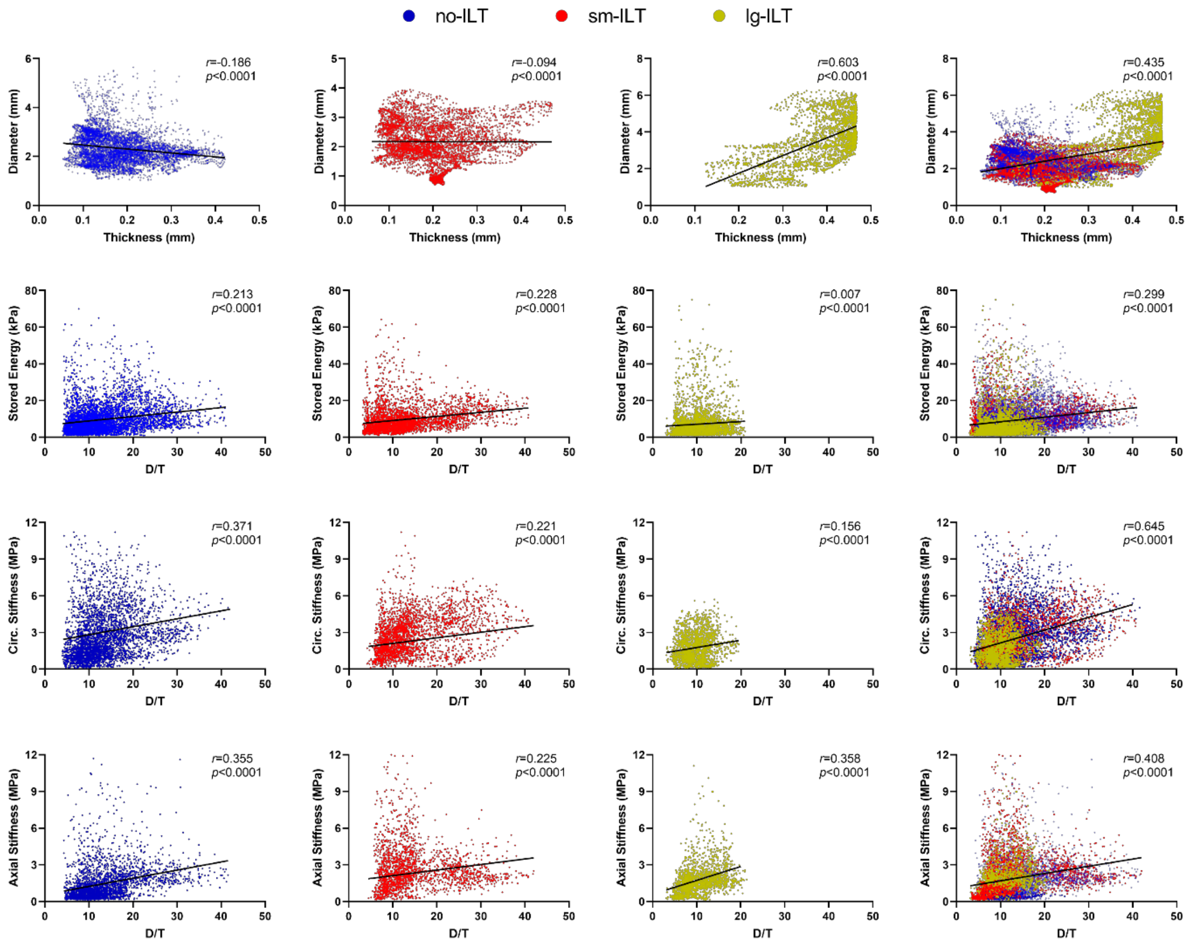

Figure S13. Possible correlations of geometric metrics (first row) as well as correlations between mechanical and geometric metrics (remaining rows). Data are shown for all 14 aneurysms that were tested *in vitro* and all computational regions (~800-1000 each) therein. Results are shown separately for the three k-means defined study groups as well as overall (right column). The non-dimensional parameter, local outer diameter (D) normalized by local wall thickness (T), appeared useful. Although all mechanical metrics were considered, shown here are three particularly relevant: stored energy (second row), circumferential material stiffness (third row), and axial material stiffness (fourth row). Correlations were performed using the non-parametric Spearman correlation coefficient, r (upper left at each panel); linear regressions are shown as well by the straight lines; possible significance of each correlation is shown via a p value. The correlations were generally stronger for the combined data (right column). All results are summarized in Figure S14.

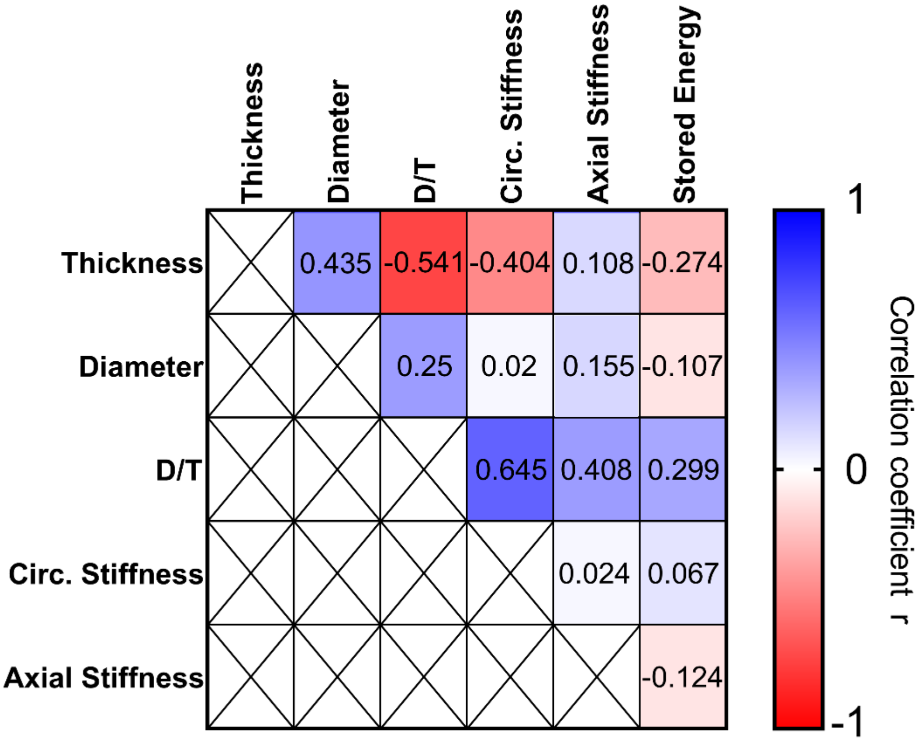

	Thickness	Diameter	D/T	Circ. Stiffness	Axial Stiffness	Stored Energy
Thickness		0.435	-0.541	-0.404	0.108	-0.274
Diameter			0.25	0.02	0.155	-0.107
D/T				0.645	0.408	0.299
Circ. Stiffness					0.024	0.067
Axial Stiffness						-0.124

Figure S14. Summary of results from Figure S13; positive and negative correlations are marked with blue and red tiles, respectively.

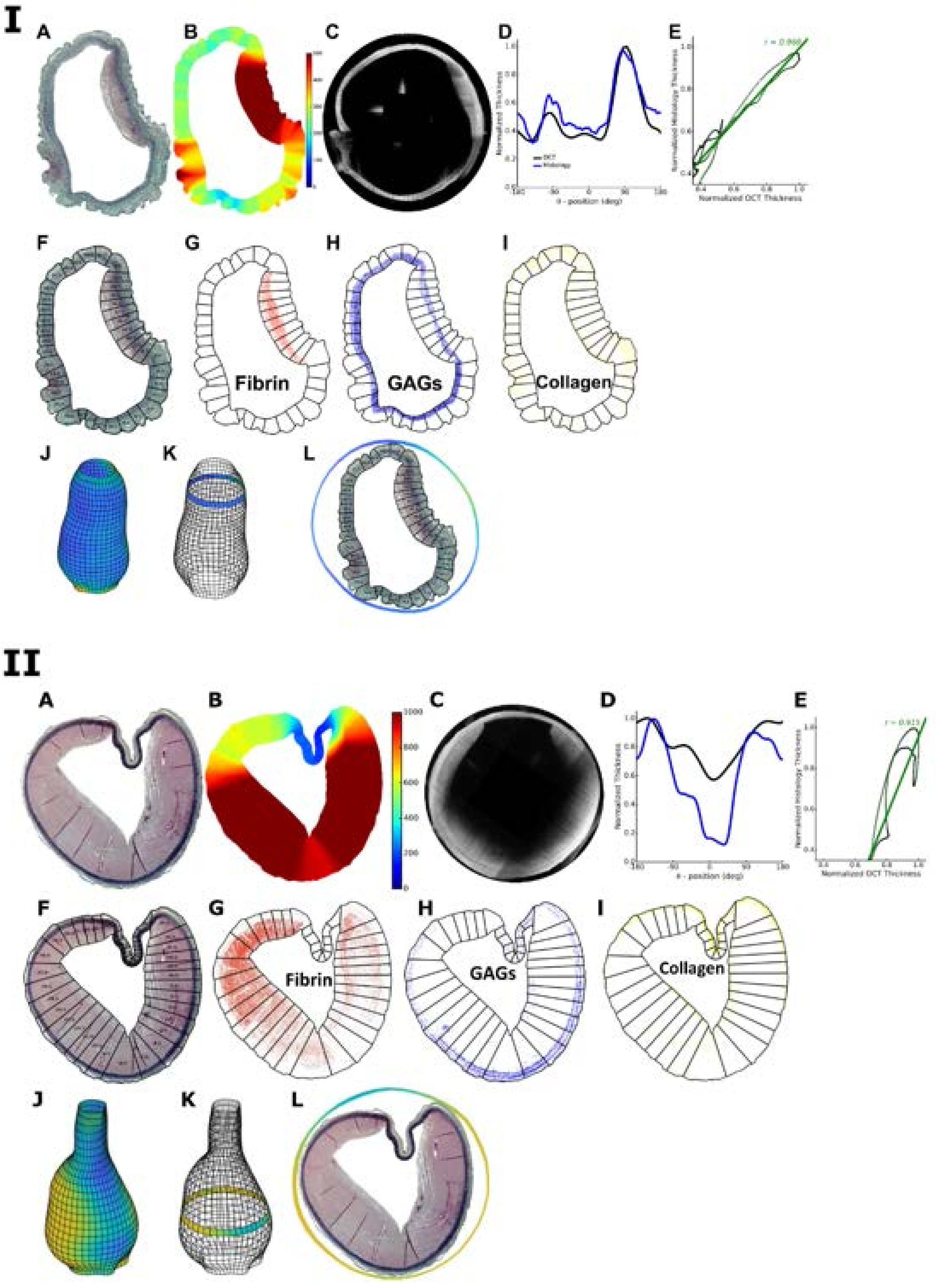

Figure S15. To facilitate local comparisons of histological findings, wall thickness (OCT), and biomechanical metrics (pDIC), histological cross-sections were divided into 40 circumferential sectors. Shown here are two representative samples (A): (I) sm-ILT and (II) lg-ILT (see Figure 5 in the main text). Circumferential variations in (B) histologically-measured and (C) OCT-measured wall thickness were (D) normalized (to account for shrinkage of histological sections and the different biomechanical states, unloaded in histology and loaded in OCT and pDIC) and (E) compared using correlation analysis to optimally co-register along the (K) reconstructed 3D vessel geometry (entire distributions are shown in J). Note that the (F) 40 histological sectors correspond numerically with the 40 computational elements along the circumferential direction in the inverse characterization (Figures S4-S12). The (G-I) histological area fractions for the different constituents were computed for each sector and (L) associated with local material properties of interest that were identified by the inverse modelling.

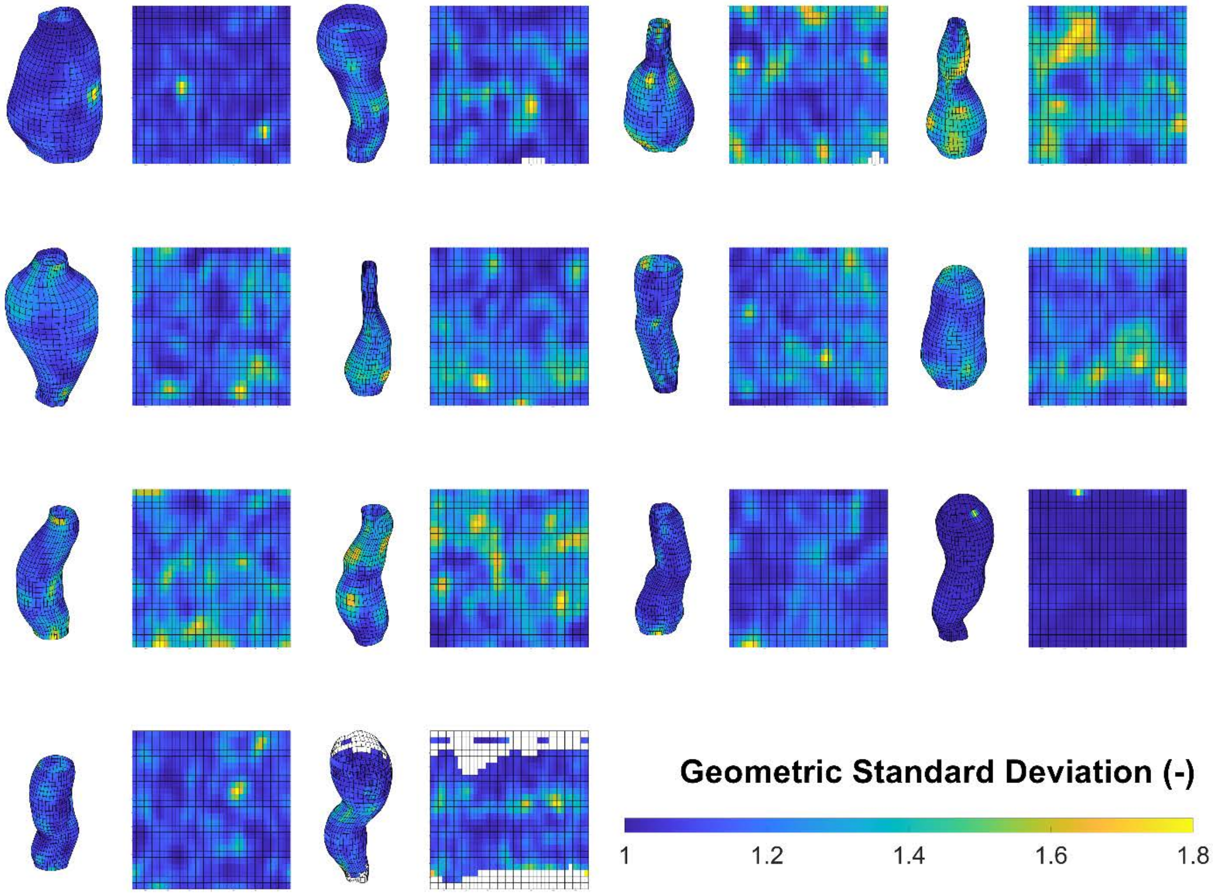

Figure S16. Specimen-specific maps of the geometric standard deviation (GSD) used as a scalar metric of relative uncertainty, shown here for circumferential material stiffness as an example. The uncertainties in material stiffness components were computed by analytically propagating the uncertainties in the individual constitutive parameters, which were themselves computed from the log-likelihood function maximized during inverse characterization. The resulting uncertainties in material stiffness were generally small (median GSD < 1.2, with 90th percentile < 1.4), indicating that these functional metrics can be estimated locally with relatively high precision (note that the lower bound GSD = 1 denotes complete certainty).

Table S1. Parameters for the computational growth and remodeling simulations for the infrarenal abdominal aorta of a healthy adult male C57BL/6J mouse determined from standard biaxial mechanical data (baseline passive response - control) as well as for longitudinal bulk data for AAAs (“no-ILT” group) at weeks 4 and 8 following elastase+BAPN exposure. “Elastin” (e), “Smooth Muscle” (m), “Collagen” (c), and “GAG/PG” (GAG) parameters represent elastin-dominated isotropic, smooth muscle / collagen-dominated anisotropic, and glycosaminoglycan-dominated isotropic contributions. Subscripts M and A refer to medial and adventitial layers, respectively; subscripts r, θ, z refer to radial, circumferential, and axial directions; subscripts σ, τ_w, W refer to mean pressure- and axial force-induced intramural (volumetric) stress, flow-induced shear stress, and stored energy. Elastin parameter c^e and (newly formed, all families) collagen parameter c_1^c were reduced 95% each following elastase and BAPN exposure, respectively, at G&R time $s = 0$. Similarly, the deposition stretch for axial collagen was increased 22.5% and parameter c_2^c of circumferential collagen was reduced 89% during remodeling.

Baseline Passive Response	
Inner, Media-Adventitia Interface, Outer Radii [μm]	398, 413, 427
Medial Mass fractions, ϕ_M^e, ϕ_M^m, ϕ_M^c, ϕ_M^{GAG} [-]	0.148, 0.626, 0.187, 0.039
Adventitial Mass fractions, ϕ_A^e, ϕ_A^c [-]	0.003, 0.997
Medial Collagen Fractions, β_{Mz}, β_{Md} [-]	0.047, 0.953
Adventitial Collagen Fractions, $\beta_{A\theta}$, β_{Az}, β_{Ad} [-]	0.111, 0.047, 0.842
Diagonal Collagen Orientation, α_0 [°]	35.9
Elastin Parameter, c^e [kPa]	144.2
Elastin Deposition Stretches, G_r^e, G_θ^e, G_z^e [-]	$1/G_\theta^e G_z^e$, 2.20, 2.24
Smooth Muscle Parameters, c_1^m [kPa], c_2^m [-]	225.5, 0.105
Collagen Parameters, c_1^c [kPa], c_2^c [-]	575.0, 2.833
Smooth Muscle / Collagen Deposition Stretches, G^m, G^c [-]	1.19, 1.16
GAG/PG Parameter, c^{GAG} [kPa]	$c^e/10$
GAG/PG Deposition Stretches, $G_r^{GAG}, G_\theta^{GAG}, G_z^{GAG}$ [-]	1.25, $1/\sqrt{G_r^{GAG}}$, $1/\sqrt{G_r^{GAG}}$
Mechano-regulated G&R	
Medial Collagen Gains, $\mathrm{K}_{M\sigma}^c$, $\mathrm{K}_{M\tau_w}^c$ [-]	1.00, 0.785
Medial Smooth Muscle Gains, $\mathrm{K}_{M\sigma}^m$, $\mathrm{K}_{M\tau_w}^m$ [-]	0.7 x ($\mathrm{K}_{M\sigma}^c$, $\mathrm{K}_{M\tau_w}^c$)
Adventitial Collagen Gains, $\mathrm{K}_{A\sigma}^c$, $\mathrm{K}_{A\tau_w}^c$ [-]	0.8 x ($\mathrm{K}_{M\sigma}^c$, $\mathrm{K}_{M\tau_w}^c$)
Mass Removal Rates, k_o^m, k_o^c, [1/day]	ln(2)/1.5, ln(2)/1.5
Energy-mediated GAG/PG Accumulation	
Mass Removal Rate, k_o^{GAG} [1/day]	ln(2)/1.2
Mass Removal Gain K_W^{GAG} [-]	0.82
Compensatory Production Characteristic Time, T^{GAG} [day]	12.5

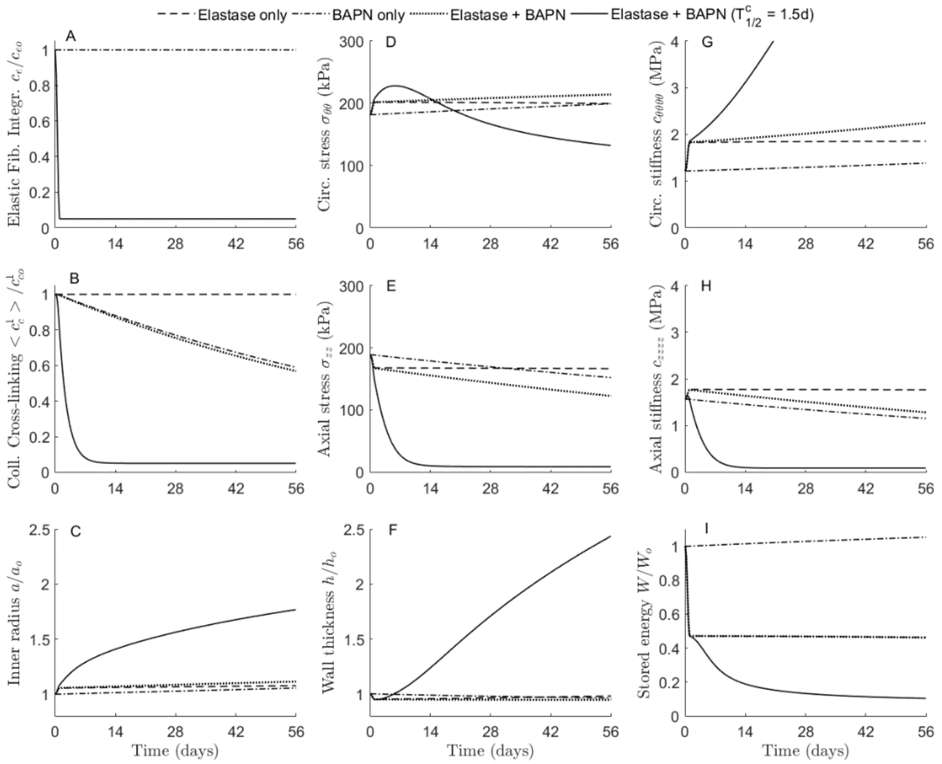

Figure S17. Initial computational growth and remodeling predictions of responses to elastase exposure alone (with a prescribed baseline half-life of collagen $T^c_{1/2} = 70$ days, dashed lines), BAPN exposure alone (with $T^c_{1/2} = 70$ days, dash-dotted), or elastase+BAPN exposure with either a baseline ($T^c_{1/2} = 70$ days, dotted) or dramatically reduced ($T^c_{1/2} = 1.5$ days, solid) half-life of collagen (see Figure 6 in the main text for panel descriptions, noting the lack of panels J-L for these initial simulations, which were performed without explicit consideration of GAGs/PGs, as in all prior implementations of the model, or additional modifications for the orientation-dependent properties of collagen fibers). Note that the marked effect of (B) BAPN on the aorta in the presence of (A) elastase is because of the marked decrease in half-life of collagen (solid lines), thus providing a biomechanical explanation for prior experimental findings (in particular, aneurysmal enlargement, C). Predictions were only qualitative at this stage (see experimental data and improved predictions when the model was augmented with GAGs/PGs in Figure 6; note the different scale in panels C and F, reduced here to compare responses to the different cases).

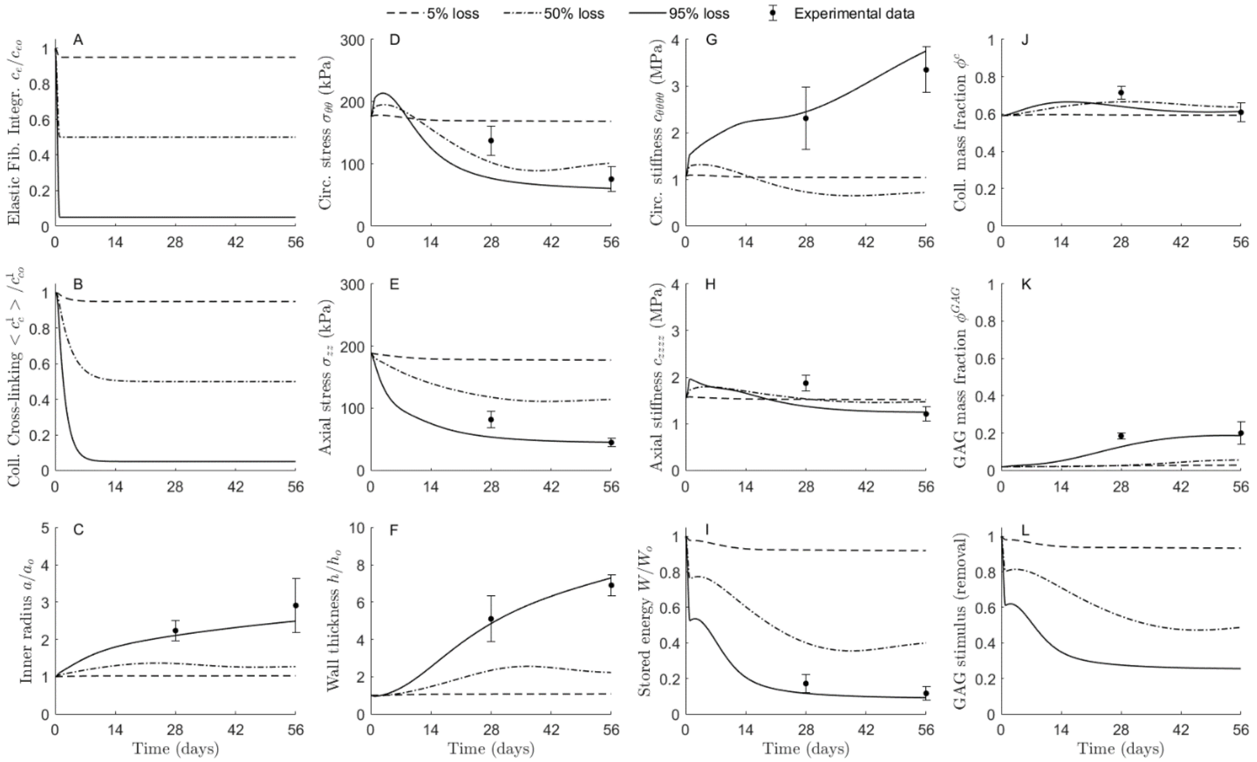

Figure S18. Same as Figure 6 in the main text, except for different degrees (5, 50, or 95%; dashed, dash-dotted, or solid lines, respectively) of simultaneous loss of (A) elastic fiber integrity and (B) cross-linking of newly deposited collagen. Note that the model predicts the experimental data (symbols) well, including (K) GAG/PG accumulation and (F) associated wall thickening, only with dramatic decreases in the corresponding parameters (c^e for structural elastin, c_1^c for collagen cross-linking). Note, too, the resulting (I) acute loss in stored energy, used herein as a surrogate metric to mediate (L) a decreased GAG/PG removal (with delayed decreased production, not shown).

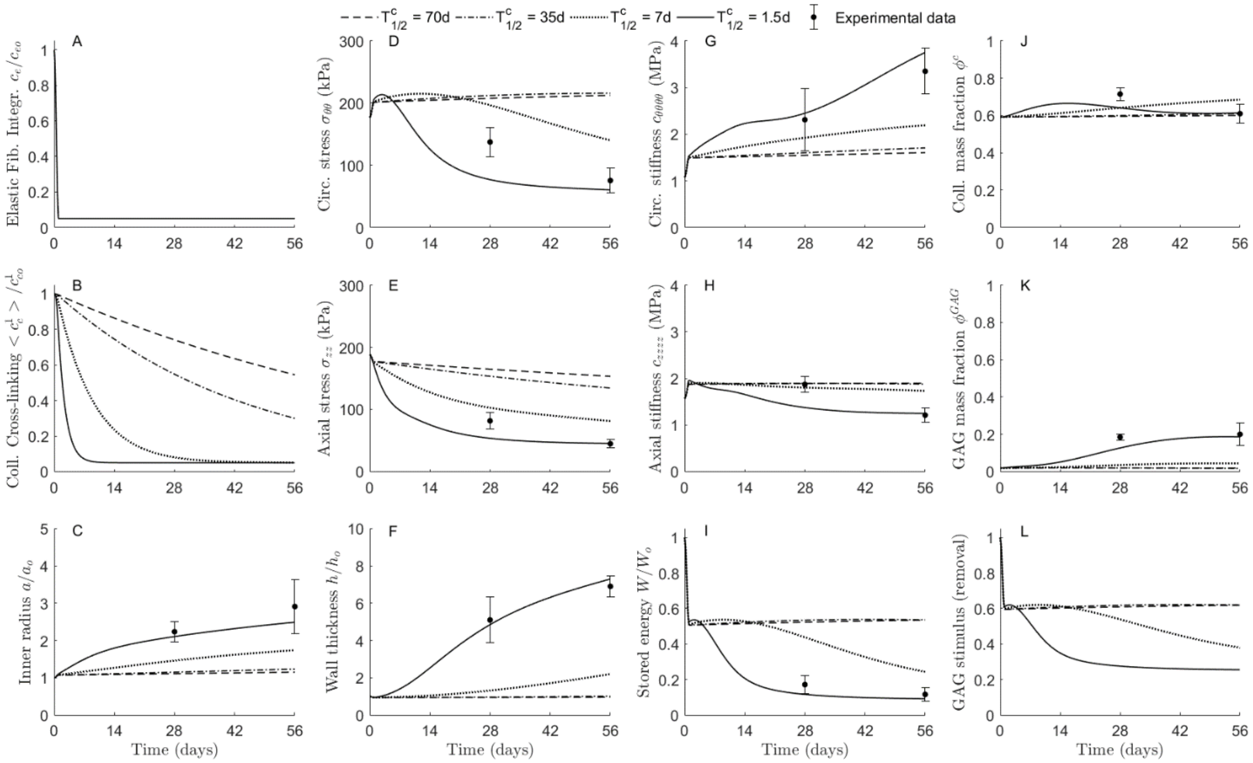

Figure S19. Same as Figure 6 in the main text, but for different half-lives of collagen $T^c_{1/2}$ (70, 35, 7, or 1.5 days; dashed, dash-dotted, dotted, or solid lines, respectively). Note that the model predicts the experimental data (symbols) well, including (K) GAG/PG accumulation and (F) associated wall thickening only for the dramatic decrease in $T^c_{1/2}$ from 70 days (baseline) to 1.5 days (solid lines), which results in (I) an early drop in stored energy, used herein as (L) a surrogate metric to mediate the decreased GAG/PG removal (with delayed decreased production, not shown).